



Aalborg Universitet

AALBORG UNIVERSITY  
DENMARK

## Optimal Performance Design Guideline of Hybrid Reference Frame based Dual-Loop Control Strategy for Stand-Alone Single-Phase Inverters

Han, Yang; Jiang, Ai-Ting; Coelho, Ernane A. A.; Guerrero, Josep M.

*Published in:*  
I E E Transactions on Energy Conversion

*DOI (link to publication from Publisher):*  
[10.1109/TEC.2017.2769114](https://doi.org/10.1109/TEC.2017.2769114)

*Publication date:*  
2018

*Document Version*  
Early version, also known as pre-print

[Link to publication from Aalborg University](#)

*Citation for published version (APA):*

Han, Y., Jiang, A-T., Coelho, E. A. A., & Guerrero, J. M. (2018). Optimal Performance Design Guideline of Hybrid Reference Frame based Dual-Loop Control Strategy for Stand-Alone Single-Phase Inverters. *I E E Transactions on Energy Conversion*, 33(2), 730-740. <https://doi.org/10.1109/TEC.2017.2769114>

### General rights

Copyright and moral rights for the publications made accessible in the public portal are retained by the authors and/or other copyright owners and it is a condition of accessing publications that users recognise and abide by the legal requirements associated with these rights.

- ? Users may download and print one copy of any publication from the public portal for the purpose of private study or research.
- ? You may not further distribute the material or use it for any profit-making activity or commercial gain
- ? You may freely distribute the URL identifying the publication in the public portal ?

### Take down policy

If you believe that this document breaches copyright please contact us at [vbn@aub.aau.dk](mailto:vbn@aub.aau.dk) providing details, and we will remove access to the work immediately and investigate your claim.

# Optimal Performance Design Guideline of Hybrid Reference Frame-based Dual Loop Control Strategy for Stand-Alone Single-Phase Inverters

Yang Han, *Senior Member, IEEE*, Ai-Ting Jiang, Ernane A. A. Coelho, and Josep M. Guerrero, *Fellow, IEEE*

**Abstract**—The dual-loop control strategy in hybrid reference frame (HRF) for single-phase voltage source inverters (VSIs) in islanded operation mode is studied, which applies a capacitor voltage shaping loop in the synchronous reference frame (SRF) and a capacitor current shaping loop in the stationary reference frame (HRF-based  $v+i_c$  control strategy). This strategy is able to achieve the purpose of active damping, fast dynamic response and zero reference tracking error. However, due to the inherent characteristics of SRF-based voltage loop and the digital control delay, the performance of the system is degraded and the control parameter design of HRF-based  $v+i_c$  control strategy shows great difficulties. To overcome these shortcomings, in this paper, a systematic parameter design guideline for HRF-based  $v+i_c$  control strategy is proposed to ensure the system stability and optimize the performance of the system under control delay condition. The mathematic model of the HRF-based  $v+i_c$  control strategy is established with the consideration of control delay in this paper. Based on this model, a satisfactory region of the system stability indexes can be obtained by stability specifications of the system and the optimal control parameters can be calculated according to the stability indexes selected from the satisfactory region. By using this method, the system stability and robustness can be guaranteed. Finally, the experimental results are presented to validate the effectiveness of the presented optimal control parameter design methodologies.

**Index Terms**—Control delay, single-phase inverter, hybrid reference frame, islanded mode, parameter design guideline.

## NOMENCLATURE

### Abbreviations

HRF	Hybrid reference frame.
VSI	Voltage source inverter.

Manuscript received April 23, 2017; revised September 26, 2017; accepted October 27, 2017. Date of publication \*\*\*\*\*, date of current version \*\*\*\*\*. This work was supported by Sichuan Province Key Research and Development Project under grant No.2017GZ0347. Paper no. TEC-00307-2017.

Y. Han and A. Jiang are with the Department of Power Electronics, School of Mechatronics Engineering, University of Electronic Science and Technology of China (UESTC), No.2006, Xiyuan Avenue, West Hi-Tech Zone, Chengdu 611731, China (e-mail: hanyang@uestc.edu.cn; 532470232@qq.com).

Ernane A.A. Coelho is with the Universidade Federal de Uberlandia, Uberlandia 38400-902, Brazil (ernane@ufu.br).

J. M. Guerrero is with Department of Energy Technology, Aalborg University, 9220 Aalborg, Denmark (e-mail: joz@et.aau.dk).

Color versions of one or more of the figures in this paper are available online at <http://ieeexplore.ieee.org>.

Digital Object Identifier \*\*\*\*\*/TEC.\*\*\*\*\*

SRF	Synchronous reference frame.
DG	Distributed generation.
PWM	Pulse-width modulation.
PR	Proportional resonant.
SRF-PI	Synchronous reference frame proportional integral.
OSG	Orthogonal signal generation.
PM	Phase margin.
GM	Gain margin.
MOSFET	Metal-oxide field effect transistor.
APF	All-pass filter.
FFT	Fast Fourier transformation.
THD	Total harmonic distortion.

### Variables

$i_L$	Inductor current.
$i_c$	Capacitor current.
$i_o$	Output current.
$v$	Output voltage.
$v_c$	Capacitor voltage.
$v_{\alpha}, v_{\beta}$	Voltage components in $\alpha\beta$ -axis.
$v_d, v_q$	Voltage components in $dq$ -axis.
$V_{dc}$	Voltage at dc-side of the VSI.
$V_{inv}$	Voltage at ac-side of the VSI.

### Parameters

$\omega_f$	Fundamental frequency.
$L$	Output inductor of inverter.
$r_L$	Series resistance of the inductor
$C$	Capacitor of the LC filter.
$R$	Load resistance.
$v_d^*, v_q^*$	Rated voltage in $dq$ -axis.
$i_{c,d}^*, i_{c,q}^*$	Rated capacitor current in $dq$ -axis.
$f_s$	Sampling frequency.
$V_{tri}$	Amplitude of the triangular carrier signal.
$f_g$	Crossover frequency at $-180^\circ$ .
$f_c$	Crossover frequency at $0$ dB.
$K_p, K_i$	Parameters of the PI controller.
$K$	Proportional value of the current controller.

## I. INTRODUCTION

Distributed generation (DG) systems, such as photovoltaic and wind power systems, are attracting increasing interest due to the high requirement of reliability and low loss of transmission and distribution networks in recent years. With the rapid development of the application of DGs, the power electronic inverters are being widely utilized to overcome the difficulties such as controlling the voltage amplitude and

frequency with a fast dynamic response and zero steady-state errors [1-4]. For the single-phase inverters, the full-bridge pulse width modulation (PWM) inverter, whose major requirement of its control system is to control the voltage to achieve the steady state with zero steady-state error and a fast dynamic response, is widely used either in grid-connected or islanded mode voltage regulators in the distributed power systems [5].

To regulate the system voltage of the single-phase inverters in islanded mode, various control strategies have been proposed in recent literatures [6]-[31]. In [6]-[9], the deadbeat control is suggested to control the load voltage parameters such as the amplitude and frequency. For its simplicity in implementation and wide control bandwidth, deadbeat control is widely used in the PWM inverters. However, the parametric sensitivity, which exists in the system due to the high-order plant controlled by the deadbeat controller, can reduce the system stability margin. In [10]-[16], the repetitive control is presented, which shows an excellent control performance for periodic signals. This feature makes it very effective for suppressing the harmonics and emulating various scenarios of power grids. However, the low-accuracy tracking performance, slow transient response and poor rejection of the aperiodic disturbances are the main limitations of the typical repetitive controller. The discrete-time sliding-mode is suggested as another control strategy to ensure the output voltage quality in [17]-[21]. The interesting feature of the discrete-time sliding-mode control is its robustness, fast transient response and simple digital implementation. Moreover, it is able to provide a direct control without any modulation schemes. Despite the aforementioned advantages, this technique suffers from some drawbacks, including the so-called chattering phenomenon resulted from the actuator limitations or time discretization, which can deteriorate the control accuracy and performance of the system. [20], [21].

The proportional-resonant (PR) control method is popular for the single-phase inverters thanks to the ability to eliminate the tracking error while regulating the AC signals [22], [23]. When tracking a sinusoidal reference, this control strategy does not require decoupling structures and it is able to ensure the system with zero steady-state error at a frequency even with the variations of the circuit parameters [24], [25]. However, the poor dynamic performance and the requirement of the very high switching frequency limit the application of this technique [26], [27]. To overcome these drawbacks, the synchronous reference frame proportional-integral (SRF-PI) controller, which is a well-developed technique in three-phase PWM converters, is taken into consideration for the single-phase inverters. In [28], [29], incorporating the SRF-PI controller into the single-phase PWM inverters is proposed, which provides the zero steady-state error through the conventional PI controller in synchronous reference frame. For this controller, two orthogonal signals are generated by the orthogonal signal generation (OSG) techniques with respect to the fundamental frequency of the single-phase signal and then transformed into the synchronous reference frame. A conventional PI regulator, which is followed by the coordinate transformation, regulates the synchronous reference frame signals to ensure a zero steady-state error and then, the signals are transformed back to

the stationary frame by an inverse Park's transformation [30], [31].

Employing a single-loop instantaneous voltage feedback control is probably the simplest way to regulate the inverter output voltage with zero steady-state error. However, in the industrial applications, a typical LC filter, which is usually incorporated into the PWM converter to suppress the harmonic contents of the output voltage from the inverter, may introduce a resonance peak and reduce the stability margin of the PWM inverters. To solve this problem, in renewable energy system applications, dual-loop control strategies are introduced into the inverters [32]. For these strategies, the inner loops, which are usually the current loops, use the current of the filter inductor or capacitor current as the feedback signal to damp the resonance peak of LC filter, and outer loops, which are normally the voltage loops, use the filter capacitor voltage as the reference signal to regulate the output voltage [33].

In [34], a dual-loop control strategy based on the hybrid reference frame is proposed, which adopts a capacitor voltage shaping loop with the SRF-PI controller and a capacitor current shaping loop in the stationary reference frame (here named HRF-based  $v+i_c$  control strategy). This control strategy is able to achieve the steady-state with zero steady-state error and actively damp the resonance peak of the LC filter. However, the control parameter design method of the HRF-based  $v+i_c$  control strategy is not comprehensive in [34] since it neglects the impact of control delay, which is mainly brought by the computation and pulse width modulated (PWM) delays [35]. It has been reported that the control delay cannot be ignored because it reduces the system phase margin and influences the system minimum phase properties [36], [37]. In [38], a systematic parameter design with control delay consideration for  $v+i_c$  control strategy is proposed, but the voltage loop applies the PR controller in the stationary frame instead of SRF-PI controller. In [39], a parameter design guideline of the control strategy working on the SRF is suggested while taking into account the control delay. Nevertheless, as for SRF-based voltage control and the parameter design of the HRF-based  $v+i_c$  control strategy under the impact of the control delay has not been fully addressed in the existing literatures.

This paper aims to provide a systematic parameter design guideline for the single-phase inverters using HRF-based  $v+i_c$  control strategy with consideration of control delay. The main contributions of this paper are summarized as follows:

- 1) This paper presents the dual-loop control strategy in the hybrid reference frame for stand-alone single-phase inverters, which applies a capacitor voltage control loop in synchronous reference frame and a capacitor current shaping loop in the stationary reference frame. The mathematic model of the single-phase inverter with this strategy is established under control delay scenario.

- 2) A systematic method for designing SRF-PI controller and current controller is proposed for the HRF-based  $v+i_c$  control strategy with consideration of the control delay. This method designs a satisfactory region, which is specified by the phase margin (PM) from  $30^\circ$  to  $60^\circ$  and the gain margin (GM) greater than 3 dB with the consideration of control delay of  $150 \mu s$ .

With this predefined region, the control parameters of the SRF-PI controller and the current controller can be easily obtained, and it is more convenient and explicit to optimize the system performance according to the satisfactory region.

3) Implementation of the HRF-based  $v+i_c$  control strategy with the designed control parameters on a single-phase inverter system has been presented to validate the effectiveness of the proposed parameter design methodologies.

This paper is organized as follows. In Section II, the control structure of the single-phase inverters with HRF-based  $v+i_c$  control strategy and the equivalent model of the SRF-PI controller in the stationary reference frame are presented. The mathematic model of the HRF-based  $v+i_c$  control strategy is established as well. In Section III, a systematic parameter design guideline for the standalone single-phase inverters using HRF-based  $v+i_c$  control strategy with consideration of control delay is proposed, which is conducted by specifying the satisfactory region of the stability indexes according to the stability margin. In Section IV, the experimental results are presented to validate the effectiveness of the proposed design approach. Finally, Section V concludes this paper.

## II. CONTROL STRUCTURE OF THE SINGLE-PHASE INVERTERS

### A. Control Structure of the Single-Phase Inverter with the HRF-based $v+i_c$ Control Strategy

Fig. 1 illustrates the control structure of the single-phase inverter using the HRF-based  $v+i_c$  control strategy operated in the islanded mode. As shown in Fig. 1, for the power circuit of the single-phase inverter, an insulated-gate bipolar transistor (IGBT) full-bridge configuration, followed by an  $LC$  filter, is set as a VSI to produce PWM sinusoidal voltage  $V_{inv}$ . A linear load is in parallel with the capacitor. In the power circuit of the single-phase inverter,  $r_L$  denotes the series resistance of the inductor,  $i_l$  denotes the inductor current,  $i_c$  denotes the capacitor current,  $i_0$  denotes the load current and  $v_c$  denotes the capacitor voltage of the LC filter.

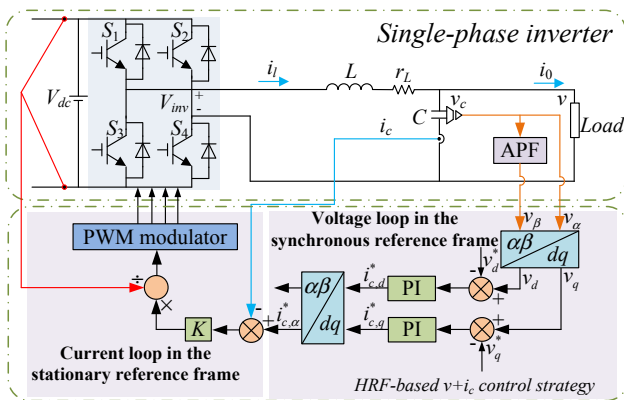


Fig. 1. The control structure of the single-phase inverter using the HRF-based  $v+i_c$  control strategy [34].

Meanwhile, the HRF-based  $v+i_c$  control strategy for the full-bridge single-phase inverter is presented in Fig. 1 as well, which includes an SRF-PI voltage controller to regulate the output voltage and a capacitor current loop in the stationary reference frame to provide active damping and fast dynamic response [34]. As shown in Fig. 1, it can be observed that the

capacitor voltage and its orthogonal signal are transformed into synchronous frame by using Park transformation, which is followed by a PI controller. It should be mentioned that, the orthogonal signal is generated by an all-pass filter (APF), which causes a  $90^\circ$  phase delay at the fundamental frequency  $\omega_f$  and has unity-gain magnitude for all frequency  $\omega$  with respect to the capacitor voltage [40]. This technique is easy to achieve and the structure of a first-order APF is illustrated in Fig. 2.

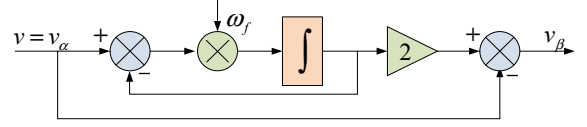


Fig. 2. The structure of a first-order APF [34].

Since only  $\alpha$ -axis quantities belong to the real system, the  $\alpha$ -axis signal is fed forward to shape the voltage loop and at the same time, as the reference signal of the inner current loop when the HRF-based  $v+i_c$  control strategy is conducted. It should be noted that the capacitor current ( $i_c$ ) is selected as the feedback signal of the inner current loop. And the controller of the inner current loop is a proportional controller instead of a PI controller, which is popular in current feedback control [41]. By applying a proportional controller, the phase delay problem can be easily solved compared to the PI controller and it is able to accelerate the dynamic response of the system.

### B. Analysis of the SRF-PI Controller

Since the voltage loop works in the synchronous reference frame, which blocks the analysis of the whole closed-loop system and the appropriate design of the control parameters, it is essential to establish an equivalent model of the SRF-PI controller in the stationary frame. In [34], the stationary reference frame equivalent of the SRF-PI controller is derived by Monfared *et al*, which gives a better insight on the single-phase inverter using the HRF-based  $v+i_c$  control strategy and has a significant effect on parameter design and stability analysis of the system.

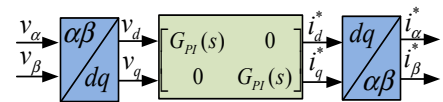


Fig. 3. The block diagram of the SRF-PI controller [34].

The block diagram of the SRF-PI controller is shown in Fig. 3, where the  $G_{PI}(s)$  denotes the transfer function of the PI controller, that is,  $G_{PI}(s) = K_p + K_i/s$ . With two inputs and two outputs, which are both in the stationary reference frame, the equivalent of the structure shown in Fig. 3 can be written in time-domain as [34]:

$$\begin{bmatrix} i_\alpha^*(t) \\ i_\beta^*(t) \end{bmatrix} = \begin{bmatrix} \cos(\omega_f t) & -\sin(\omega_f t) \\ \sin(\omega_f t) & \cos(\omega_f t) \end{bmatrix} \begin{bmatrix} G_{PI}(t) & 0 \\ 0 & G_{PI}(t) \end{bmatrix} * \begin{bmatrix} \cos(\omega_f t) & \sin(\omega_f t) \\ -\sin(\omega_f t) & \cos(\omega_f t) \end{bmatrix} \begin{bmatrix} v_\alpha(t) \\ v_\beta(t) \end{bmatrix} \quad (1)$$

where  $*$  denotes the convolution.

Taking the Laplace transform from both sides of (1) and substituting the transfer function of PI controller yield [34]:

$$i_c^*(s) = \frac{a_3 s^3 + a_2 s^2 + a_1 s + a_0}{s^3 + \omega_f s^2 + \omega_f^2 s + \omega_f^3} v_\alpha(s) = H(s) v_\alpha(s) \quad (2)$$

where

$$\begin{cases} a_3 = K_p, & a_2 = K_p \omega_f + K_i \\ a_1 = K_p \omega_f^2 + 2\omega_f K_i, & a_0 = K_p \omega_f^3 - \omega_f^2 K_i \end{cases} \quad (3)$$

Hence, the  $H(s)$  is the transfer function of the SRF-PI controller in the stationary reference frame, which has a significant influence on facilitating the analysis of the whole system and designing the control parameters of the inverter.

### C. Mathematic Model of the HRF-based $v+i_c$ Control Strategy

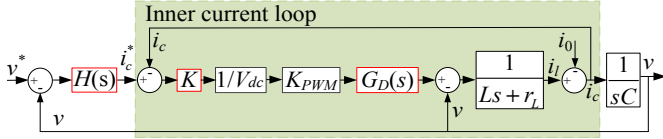


Fig. 4. Control scheme of the HRF-based  $v+i_c$  control strategy in the stationary reference frame.

Fig. 4 illustrates the control scheme of the HRF-based  $v+i_c$  control strategy in the stationary reference frame.  $K_{pwm}$  is the transfer function of PWM inverter, which is defined as  $V_{dc}/V_{tri}$ , where  $V_{dc}$  is the amplitude of the input dc voltage and  $V_{tri}$  is the amplitude of the triangular carrier signal [42].  $G_D(s)$  denotes the transfer function of the control delay for this system, which can be expressed as  $e^{-T_d s}$  with  $T_d=1.5/f_s$  and  $f_s=10$  kHz [38]. Generally, the form of the  $G_D(s)$  has three approximations, and to acquire a high bandwidth for the inverter in islanded mode, the approximation shown as (4) is preferred [38].

$$G_D(s) = e^{-T_d s} = \frac{1 - \frac{T_d}{2} s}{1 + \frac{T_d}{2} s} \quad (4)$$

Assuming that the linear load resistance is  $R$  and the  $i_0$  in the block diagram of Fig. 4 can be expressed as:

$$i_0 = v / R \quad (5)$$

In addition, according to [35], the amplitude of the triangular carrier signal  $V_{tri}$  is set as 1 pu. Hence, combining with (5) and  $K_{pwm} = V_{dc}/V_{tri}$ , the closed-loop transfer function of the inner current loop can be written as:

$$\begin{aligned} \frac{i_c}{i_c^*} = G_i(s) &= \frac{K \cdot 1 / V_{dc} \cdot K_{pwm} G_D RCs}{LRCs^2 + KG_D RCs + r_L RCs + Ls + r_L + R} \\ &= \frac{KG_D RCs}{LRCs^2 + KG_D RCs + r_L RCs + Ls + r_L + R} \end{aligned} \quad (6)$$

Hence, the block diagram of the HRF-based  $v+i_c$  control strategy can be simplified as Fig. 5.

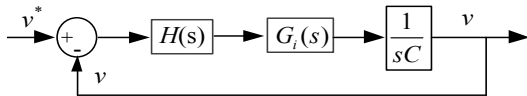


Fig. 5. The block diagram of the HRF-based  $v+i_c$  control strategy.

From Fig. 5, the open-loop transfer function of the block diagram of the HRF-based  $v+i_c$  control strategy can be expressed as:

$$G_{open}(s) = H(s) \cdot \frac{K \cdot G_D \cdot R}{LRCs^2 + KG_D RCs + r_L RCs + Ls + r_L + R} \quad (7)$$

With the above analysis, it is evident that the design of the control parameters is of vital significance to ensure the stability and optimal performance of the standalone inverter system.

### III. PROPOSED PARAMETER DESIGN GUIDELINES

Since no parameter design guideline has been proposed for the single-phase inverters with HRF-based  $v+i_c$  control strategy under control delay consideration, in this section, the design method of the control parameters is presented in detail. The presented approach is conducted by specifying the available region of the stability indexes, which is obtained according to the constraint of stability margin. With the particular region, the satisfactory stability indexes can be determined and the control parameters can be calculated with the selected stability indexes.

Fig. 6 illustrates the bode diagram of  $H(s)$  for different values of  $K_i$  with  $K_p=1$ . It can be observed that the value of  $K_i$  has no influence on the magnitude and phase frequency properties of the  $H(s)$  at the high frequency range. Since the stability margins, corresponding to the phase margin (PM) and the gain margin (GM), are both defined at the high frequencies, the  $K_i$  can be selected as zero to simplify the  $H(s)$ , which yields:

$$H(s) \approx K_p \quad (8)$$

Hence, the open loop transfer function of the HRF-based  $v+i_c$  control strategy can be simplified as:

$$G_{open}(s) = \frac{K_p \cdot K \cdot G_D \cdot R}{LRCs^2 + KG_D RCs + r_L RCs + Ls + r_L + R} \quad (9)$$

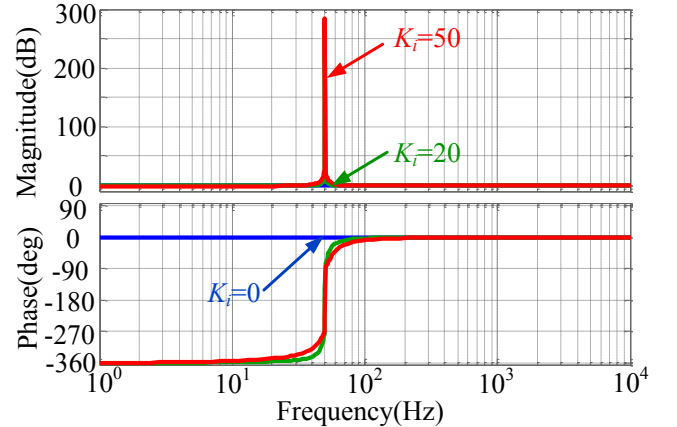


Fig. 6. The bode diagram of the  $H(s)$  with different values of  $K_i$ .

When designing a stable system, the phase should be above  $-180^\circ$  when the magnitude curve across 0 dB at the crossover frequency  $f_c$  on the bode diagram to ensure  $PM > 0$ , and the magnitude should be below 0 dB when the phase curve across  $-180^\circ$  at the frequency  $f_g$  on the bode diagram to ensure  $GM > 0$  [35]. The expressions of the PM and GM can be written as [35]:

$$PM = 180^\circ + \arctan \angle G_{open}(j\omega) \Big|_{\omega=2\pi f_c} \quad (10)$$

$$GM = -20 \lg |G_{open}(j\omega) \Big|_{\omega=2\pi f_g} \quad (11)$$

Substituting  $s=j\omega$  into (9) yields:

$$G_{open}(j\omega) = \frac{K_p KR(1 - jA_1)}{A_2 + jA_3} \quad (12)$$

where the parameters  $A_1$ ,  $A_2$  and  $A_3$  are denoted as:

$$A_1 = \frac{T_d}{2} \omega \quad (13)$$

$$A_2 = r_L + R - LRC\omega^2 + KRC \frac{T_d}{2} \omega^2 - r_L RC \frac{T_d}{2} \omega^2 - L \frac{T_d}{2} \omega^2 \quad (14)$$

$$A_3 = KRC\omega + r_L RC\omega + L\omega + r_L \frac{T_d}{2} \omega + R \frac{T_d}{2} \omega - LRC \frac{T_d}{2} \omega^3 \quad (15)$$

Hence, the phase angle and the magnitude of the open-loop transfer function can be expressed as:

$$\angle G_{open}(j\omega) = \arctan \frac{A_1 A_2 + A_3}{A_1 A_3 - A_2} \quad (16)$$

$$|G_{open}(j\omega)| = K_p KR \sqrt{\frac{A_1^2 + 1}{A_2^2 + A_3^2}} \quad (17)$$

Since the phase curve cross  $-180^\circ$  at  $f_g$ , it can be obtained that

$$(A_1 A_2 + A_3)|_{\omega=2\pi f_g} = 0 \quad (18)$$

Therefore, according to (18) and combining with (13), (14) and (15), the parameter  $K$  can be calculated as:

$$K = \frac{-L - T_d(r_L + R) - CRr_L + B_1 f_g^2}{CR + \pi^2 CRT_d^2 f_g^2} \quad (19)$$

where the variable  $B_1$  is denoted as:

$$B_1 = \pi^2 r_L CRT_d^2 + \pi^2 T_d^2 L + 4\pi^2 CLRT_d \quad (20)$$

From (19), it can be inferred that the  $K$  is proportional to  $f_g$ , which means that once the appropriate  $f_g$  is selected, the control parameter  $K$  can be easily determined.

TABLE I  
PARAMETERS OF THE INVERTER

Symbol	Values
DC Link Voltage ( $V_{dc}$ )	50V
Sampling and switching period( $T_s$ )	100 $\mu$ s
Fundamental frequency ( $\omega_0$ )	100 $\pi$ rad/s
Filter Inductance ( $L$ )	4000 $\mu$ H
Filter Capacitance ( $C$ )	2.2 $\mu$ F
ESR of the Inductor ( $r_L$ )	0.1 $\Omega$
Control delay ( $T_d$ )	150 $\mu$ s

Using the parameters listed in TABLE I, substituting (16) and (19) into (10), the relationship among the PM,  $f_c$  and  $f_g$  can be obtained, which is illustrated in Fig. 7. In industrial application, the PM is preferred to be  $30^\circ \sim 60^\circ$  to achieve a good tradeoff between the system dynamic response and the requirement of a strong robustness. According to this, when considering the control delay, which is 150  $\mu$ s in this paper, the available region constrained by PM=30 $^\circ$  and PM=60 $^\circ$  can be specified as the shadowed area shown in Fig. 7.

Similarly, at the crossover frequency  $f_c$ , the magnitude of the system can be written as

$$|G_{open}(s)|_{s=j2\pi f_c} = 1 \quad (21)$$

Substituting (21) into (17), it can be obtained that:

$$K_p = \frac{\sqrt{D_1^2 + D_2^2}}{KR \sqrt{\pi^2 T_d^2 \omega_c^2 + 1}} \quad (22)$$

where the parameters  $D_1$  and  $D_2$  are denoted as:

$$D_1 = [2\pi L + (r_L + R)\pi T_d + 2\pi(r_L + K)CR]f_c - 4\pi^3 CLRT_d f_c^3 \quad (23)$$

$$D_2 = r_L + R - 2\pi^2 T_d L f_c^2 - 4\pi^2 CLR f_c^2 + 2\pi^2 (K - r_L) CRT_d f_c^2 \quad (24)$$

From (22), it can be concluded that the  $K_p$  is related to  $K$  and  $f_c$ . Hence, once the appropriate  $K$  and  $f_c$  are selected, the control parameter  $K_p$  can be determined.

Substituting (17), (19) and (22) into (11), the relationship among the GM,  $f_c$  and  $f_g$  can be obtained, which is illustrated in Fig. 8 to give a straightforward view. To ensure the stability of the system, the satisfactory region about GM is constrained by GM=3 dB.

In Fig. 8, the satisfactory region constrained by GM $\geq$ 3 dB with control delay consideration is shown by the shadowed area, which is convenient to select the optimal  $f_c$  and  $f_g$ .

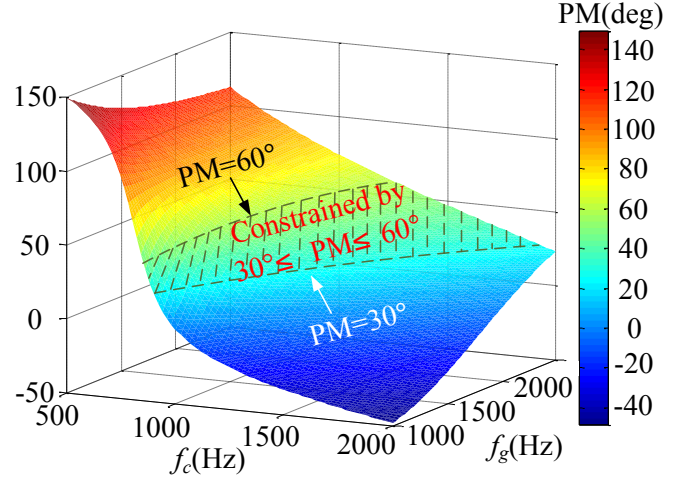


Fig. 7. The relationship of  $f_c$ ,  $f_g$  and PM.

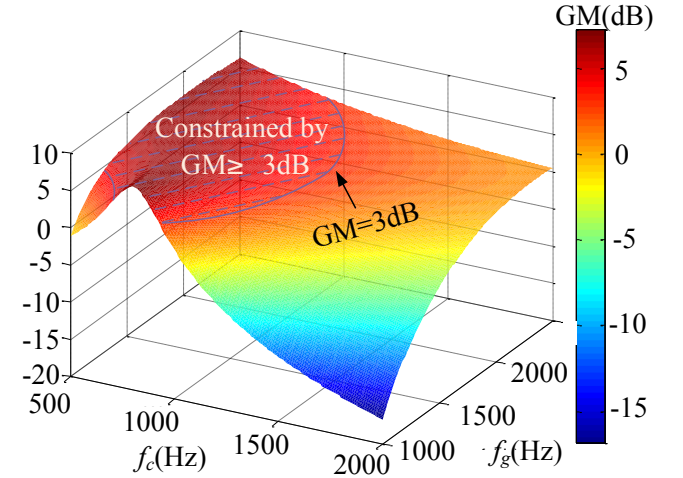


Fig. 8. The relationship of  $f_c$ ,  $f_g$  and GM.

Moreover, the  $K$  and  $K_p$  of the system should be positive. And the relationship of the  $K_p$ ,  $f_c$  and  $f_g$  is illustrated in Fig. 9. From Fig. 9, it can be observed that when  $f_g$  is equal to 1910 Hz, different  $K_p$  can be obtained from 3.32 to 7.14 with the variations of  $f_c$ . When  $f_g > 1910$  Hz, the values of  $K_p$  are between 0 and 2 and when  $f_g < 1910$  Hz, the values of  $K_p$  are negative. For the control parameter  $K$ , since it is proportional to  $f_g$ , when  $f_g$  is greater than 1907, the value of  $K$  is greater than 0.

According to the above analysis, the satisfactory region of  $f_g$  and  $f_c$  can be determined, which is plotted in the shadow in Fig. 10. In Fig. 10, point A is selected in the satisfactory region with

$f_c = 1110$  Hz and  $f_g = 1916$  Hz. Substituting the selected  $f_c$  and  $f_g$  into (19) and (22), respectively, yields:

$$K=0.89, K_p=1.71 \quad (25)$$

Moreover, as shown in Fig. 10, point B, C and D are selected on the edge of the satisfactory region. Point E and F are selected out of the region, which are out of the constraint line about  $K$  and  $K_p$  and the constraint line about PM and GM, respectively.

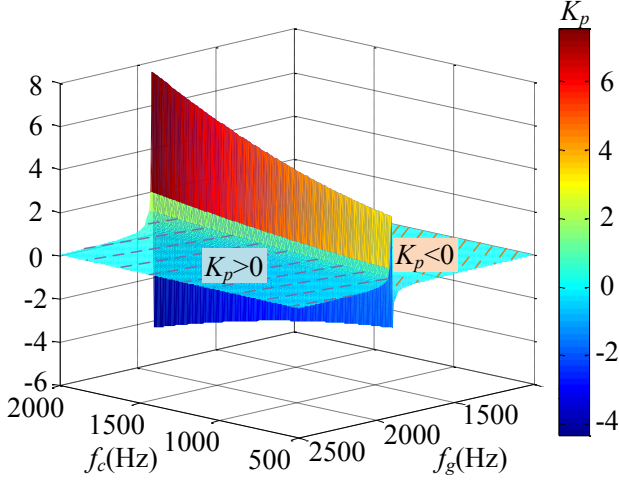


Fig. 9. The relationship of  $f_c$ ,  $f_g$  and  $K_p$ .

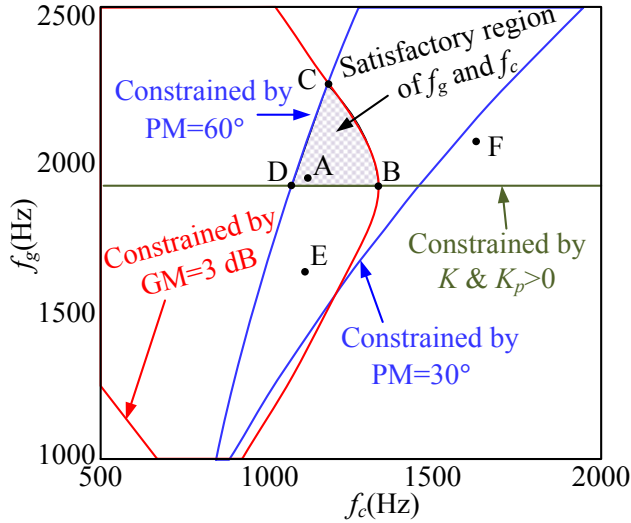


Fig. 10. The satisfactory region of  $f_g$  and  $f_c$ .

The corresponding system performance indexes of Point B, C, D, E and F are shown in Table II. From the indexes of point B, C and D, it can be obtained that the max range of  $f_c$  is from 1070 Hz to 1310 Hz and with the increase of  $f_g$ , the range of  $f_c$  decreases. Point E satisfies the specifications of the stable margin with  $PM=41.88^\circ$  and  $GM=3.94$  dB, but the values of  $K$  and  $K_p$  are negative. Point F results positive  $K$  and  $K_p$ , but the PM and GM are smaller than  $30^\circ$  and 3 dB, respectively, which are consistent with the theoretical analysis.

TABLE II  
SYSTEM PERFORMANCE INDEXES

	Point A	Point B	Point C	Point D	Point E	Point F
$f_c$ (Hz)	1110	1310	1170	1070	1170	1650
$f_g$ (Hz)	1916	1910	2260	1910	1670	2120
$K$	0.89	0.34	30	0.33	-23	19
$K_p$	1.71	5.06	0.07	4.40	-0.06	0.12
PM(deg)	57.50	40.71	60.82	60.85	41.88	26.60
GM(dB)	4.04	3.04	3.00	4.25	3.94	1.54

For the control parameter  $K_i$ , as mentioned earlier, it mainly affects the magnitude at the fundamental frequency instead of the stability of the system. Hence,  $K_i$  is selected as 10 to ensure the zero steady-state error at the fundamental frequency.

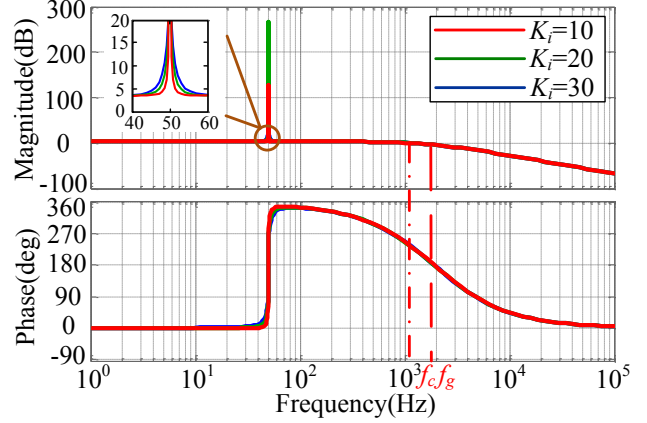


Fig. 11. The bode diagram of the open loop transfer function of the system with  $K=0.89$ ,  $K_p=1.71$  and different  $K_i$ .

Fig. 11 illustrates the bode diagram of the open loop transfer function of the system with  $K=0.89$ ,  $K_p=1.71$  and different  $K_i$ . It can be observed that all the cases are able to guarantee the stability of the system with zero steady-state error and  $K_i=10$  has the optimal filtering performance around the fundamental frequency. Moreover, when  $K_i=10$ , the crossover frequency  $f_c$  of the system is 1110 Hz,  $f_g$  is 1916 Hz, PM is  $57.50^\circ$  and GM is 4.04 dB, which all satisfy the aforementioned specifications.

According to the above analysis, the step-by-step parameter design method can be summarized as:

Step 1: Specify the phase margin and the gain margin of the system, determine the satisfactory region of  $f_c$  and  $f_g$  according to (10), (11) and define  $K>0$  and  $K_p>0$ ;

Step 2: Choose the optimal values of  $f_c$  and  $f_g$  from the satisfactory region;

Step 3: Calculate the control parameter  $K$  and  $K_p$  with the selected  $f_c$  and  $f_g$  according to (19) and (22);

Step 4: Choose a proper  $K_i$  and validate the selected  $K_i$ .

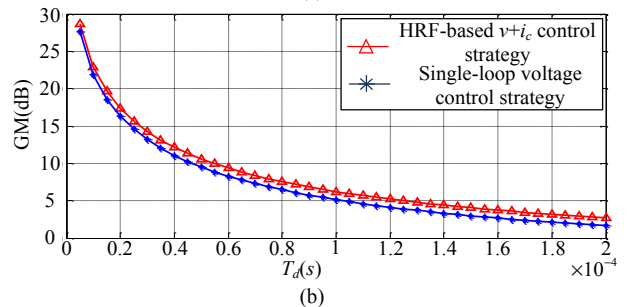
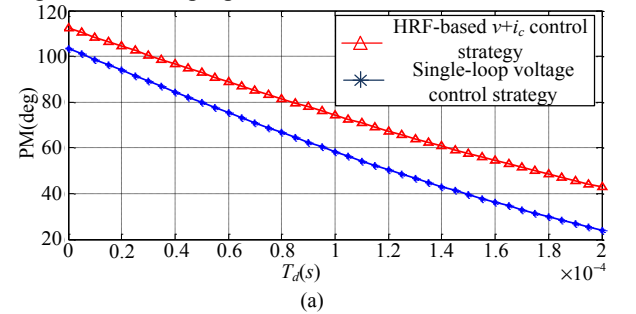


Fig. 12. The variation tendencies of the PM and GM of the systems.

Fig. 12 illustrates the variation tendencies of the PM and GM of the systems using the HRF-based  $v+i_c$  control strategy and single-loop voltage control strategy, respectively, with respect to the system delay  $T_d$  variation. It can be observed that the PM and GM of both systems decrease when  $T_d$  increases. However, when  $T_d$  increases to  $180 \mu\text{s}$ , the PM and GM of the system using single-loop voltage control strategy are smaller than  $30^\circ$  and 3 dB, respectively, while the system using HRF-based  $v+i_c$  control strategy remains a good stability margin with a PM of about  $44^\circ$  and a GM of about 4 dB.

#### IV. EXPERIMENTAL EVALUATION

To evaluate the effectiveness of the HRF-based  $v+i_c$  control strategy with the designed control parameters, a downscaled single-phase inverter system is set up, which consists of a power dc source of 50V, a full-bridge MOSFET power module, an LC filter, gate drivers and sensors. The control algorithm is implemented in TMS320F28335 controller and the reference signal of  $d$ -axis in synchronous reference frame is set to 40V.

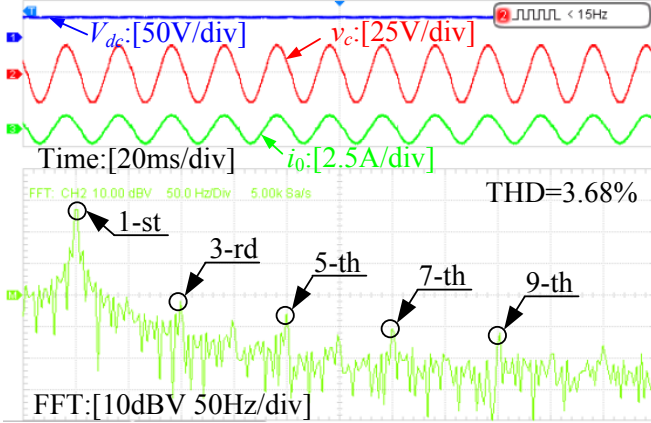


Fig. 13. Experimental waveforms of the steady-state performance of the inverters when  $K=0.89$ ,  $K_p=1.71$  and  $K_i=10$  under nominal load ( $R=20\Omega$ ).

In the first case, the steady-state performance and transient performance of the inverter with  $K=0.89$ ,  $K_p=1.71$  and  $K_i=10$  are investigated, which are shown in Fig. 13 and Fig. 14, respectively. In these figures, the channel 1 shows the DC link voltage  $V_{dc}$ , channel 2 shows the capacitor voltage  $v_c$  and channel 3 shows the load current  $i_o$ .

In Fig. 13, it can be observed that the system achieves an excellent steady-state performance and the reference voltage can be tracked accurately by the output voltage of the system. The harmonic spectrum is shown as well. From the fast Fourier transformation (FFT) analysis, it can be obtained that the total harmonic distortion (THD) under this situation is 3.68%, which shows a satisfied performance under this scenario.

Fig. 14 illustrates the transient performance of the inverter with  $K=0.89$ ,  $K_p=1.71$  and  $K_i=10$ . Fig. 14 (a) shows the transient waveforms in response to turning on the inverter. As shown in Fig. 14 (a), the system tracks the reference voltage in 4 ms with slight overshoot of about 2V during the transient process, which shows a fast dynamic response and a strong robustness. Fig. 14 (b) shows the transient response of the inverter from nominal load to 200% nominal load condition. It can be observed that during the transient process, slight ripples occur and the system achieves the steady-state in 3 ms, which shows a fast transient performance as well.

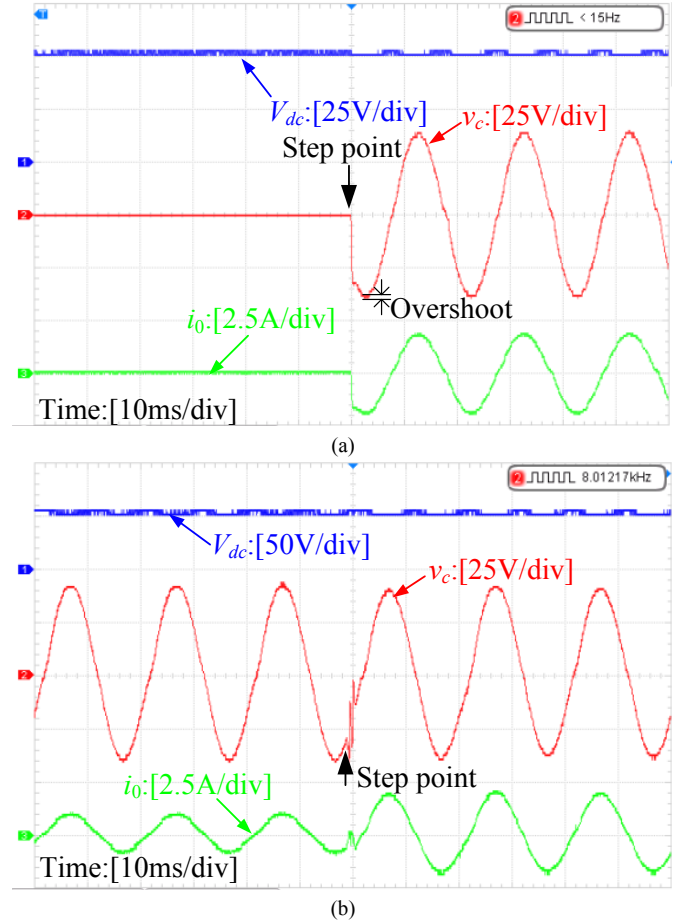
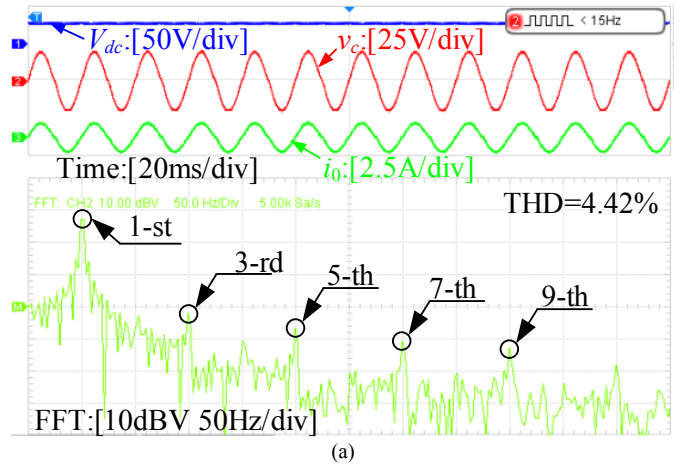


Fig. 14. Experimental waveforms of transient performance of the inverter when  $K=0.89$ ,  $K_p=1.71$  and  $K_i=10$  (a) transient waveforms in response to turning on the inverter; (b) transient waveforms undergoes nominal load to 200% nominal load step change.

Then, the steady-state performance and transient response of the inverter with  $K=19$ ,  $K_p=0.12$ ,  $K_i=10$ , which corresponding to the point F in Section III, are investigated in Fig. 15 (a) and (b), respectively. From Fig. 15, it can be observed that the THD of the system under the steady state is 4.42% and the transient response time is about 7 ms, which mean that compared to the case when  $K=0.89$ ,  $K_p=1.71$  and  $K_i=10$ , the parameters corresponding to point F can also achieve the steady-state but with a relatively poor performance on the stability and the transient response.





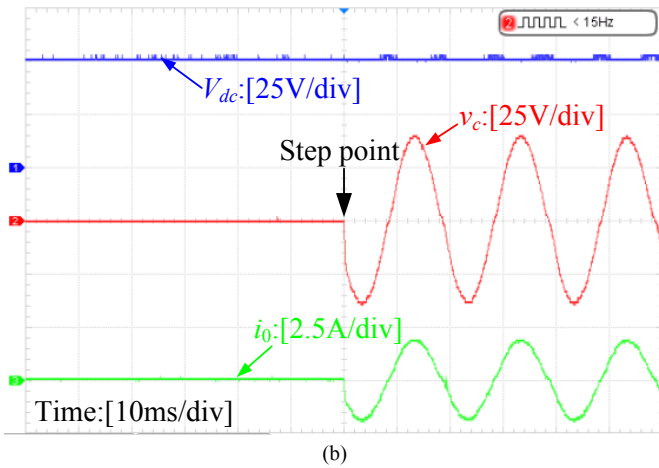


Fig. 15. Experimental waveforms of the inverter when  $K=19$ ,  $K_p=0.12$  and  $K_i=10$  (a) the steady-state performance; (b) transient performance in response to turning on the inverter.

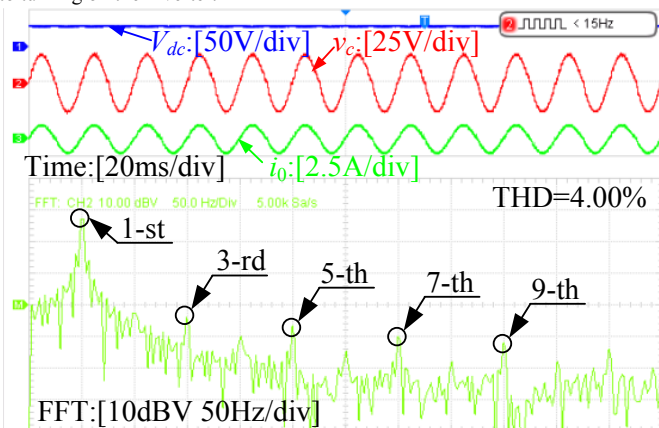


Fig. 16. Experimental waveforms of the steady-state performance of the inverter when  $K=0.89$ ,  $K_p=2$  and  $K_i=10$ .

Fig. 16 illustrates the experimental waveforms of the steady-state performance of the inverter when  $K_p$  increases. In Fig. 16,  $K_p$  is increased to 2 and it can be observed that slight oscillations appear in the capacitor voltage and the load current with the voltage THD of about 4.00% under this scenario.

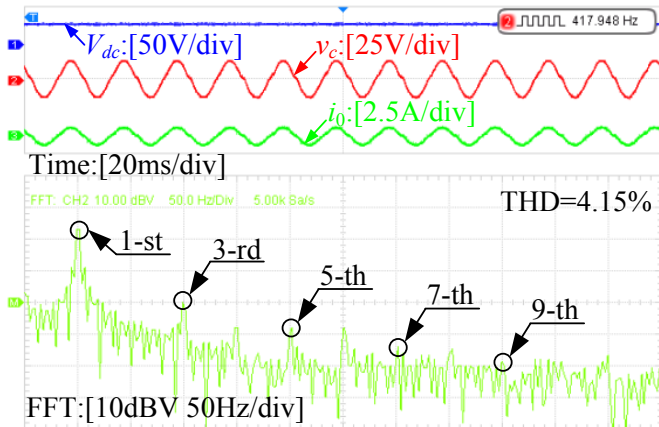


Fig. 17. Experimental waveforms of the steady-state performance of the inverter with  $K=0.7$ ,  $K_p=1.71$  and  $K_i=10$ .

The effectiveness of the selected  $K$  is evaluated as follows. The experimental waveforms of the steady-state performance of the inverter when  $K$  decreases and increases are shown in Fig.

17 and Fig. 18, respectively. As shown in Fig. 17, when  $K$  decreases, the capacitor voltage can not track the reference voltage accurately and the corresponding THD is 4.15%. When  $K$  increases, which is shown in Fig. 18, the waveforms of  $v_c$  and  $i_o$  is distorted with the voltage THD of 4.74%, which means that the inverter is slightly oscillating.

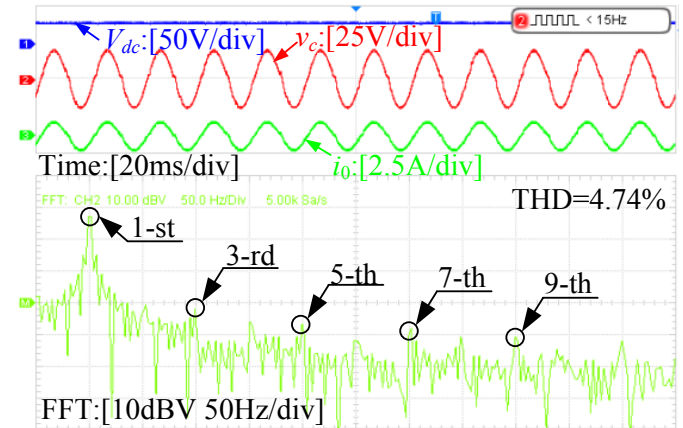


Fig. 18. Experimental waveforms of the steady-state performance of the inverter with  $K=1.2$ ,  $K_p=1.71$  and  $K_i=10$ .

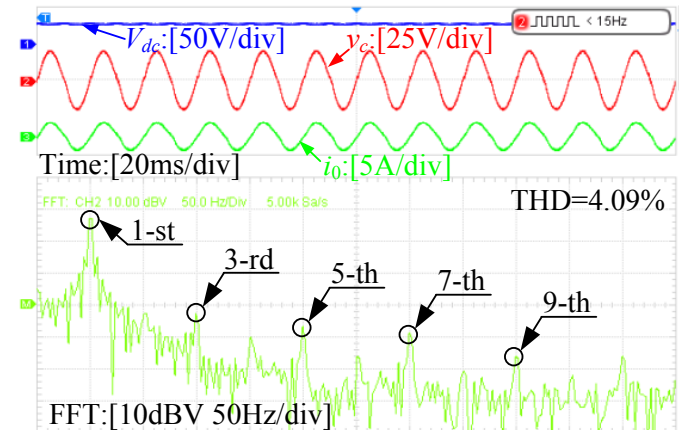


Fig. 19. Experimental waveforms of the steady-state performance of the inverters with  $K=0.89$ ,  $K_p=1.71$  and  $K_i=10$  under RL load ( $R=10\Omega$ ,  $L=3.8\text{mH}$ ).

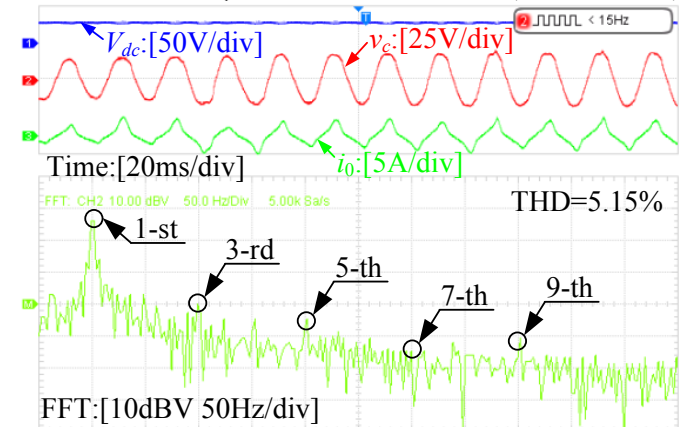


Fig. 20. Experimental waveforms of the steady-state performance of the inverters with  $K=0.89$ ,  $K_p=1.71$  and  $K_i=10$  under nonlinear load ( $L=3.8\text{mH}$ ,  $C=2000\mu\text{F}$ ,  $R=50\Omega$ ).

Finally, the steady-state performance of the inverters with  $K=0.89$ ,  $K_p=1.71$  and  $K_i=10$  under RL load and nonlinear load is studied. Fig. 19 shows that the single-phase inverter is able to achieve the steady state under RL load conditions and the THD

of the system under this situation is 4.09%. Fig. 20 shows the system performance under the nonlinear load conditions. It can be observed that the system achieves the steady state with the THD of 5.15%, which shows a good performance with the designed parameters.

## V. CONCLUSION

This paper investigates the HRF-based  $v+i_c$  control strategy for stand-alone single-phase inverters which applies a capacitor voltage loop with the PI controller in the SRF and a capacitor current loop with the proportional controller in the stationary reference frame. Taking account of control delay, the control structure of the HRF-based  $v+i_c$  control strategy is analyzed in detail, and the parameter design guideline for the SRF-PI controller for the voltage loop and the proportional controller for the current loop is presented. Moreover, the mathematic model of the HRF-based  $v+i_c$  control strategy is established taking into account the control delay.

To achieve optimal performance of the system, a detailed parameter design guideline is proposed for the HRF-based  $v+i_c$  control strategy for the SRF-PI controller and the proportional controller under condition of the control delay. By specifying the phase margin and the gain margin of the system, the satisfactory region of the stability indexes can be obtained. And the control parameters can be calculated with the stability indexes selected from the region. With the designed parameters, the system has a fast transient response and a strong robustness against the time delay. The experimental results are presented to validate the effectiveness of the parameter design method, which can be widely applied for the single-phase inverters of DGs in the islanded mode.

## REFERENCES

- [1] A. M. Egwebe, M. Fazeli, P. Igic and P. M. Holland, "Implementation and stability study of dynamic droop in islanded microgrids," *IEEE Trans. Energy Convers.*, vol. 31, no. 3, pp. 821-832, Sept. 2016.
- [2] K. Jia, H. Wei, T. Bi, D. W. P. Thomas, and M. Sumner, "An islanding detection method for multi-DG systems based on high-frequency impedance estimation," *IEEE Trans. Sustain. Energy*, vol. 8, no. 1, pp. 74-83, Jan. 2017.
- [3] M. Hamzeh, N. Rashidirad, K. Sheshyekani and E. Afjei, "A new islanding detection scheme for multiple inverter-based DG systems," *IEEE Trans. Energy Convers.*, vol. 31, no. 3, pp. 1002-1011, Sept. 2016.
- [4] H. Ghoddami and A. Yazdani, "A mitigation strategy for temporary overvoltages caused by grid-connected photovoltaic systems," *IEEE Trans. Energy Convers.*, vol. 30, no. 2, pp. 413-420, June 2015.
- [5] X. Guo, and Josep M. Guerrero, "General unified integral controller with zero steady-state error for single-phase grid connected inverters," *IEEE Trans. Smart Grid.*, vol. 7, no. 1, pp. 74-83, Jan. 2016.
- [6] W. S. Song, J. P. Ma, L. Zhou, and X. Y. Feng, "Deadbeat predictive power control of single-phase three-level neutral-point-clamped converters using space-vector modulation for electric railway traction," *IEEE Trans. Power Electron.*, vol. 31, no. 01, pp. 721-732, Jan. 2016.
- [7] M. Pichan, H. Rastegar, and M. Monfared, "Deadbeat control of the stand-alone four-leg inverter considering the effect of the neutral line inductor," *IEEE Trans. Ind. Electron.*, vol. 64, no. 4, pp. 2592-2601, Sep. 2017.
- [8] J. S. Lee, and R. D. Lorenz, "Robustness analysis of deadbeat-direct torque and flux control for IPMSM drives," *IEEE Trans. Ind. Electron.*, vol. 63, no. 5, pp. 2775-2784, May 2016.
- [9] Y. B. He, H. S. Chung, C. N. Ho, and W. M. Wu, "Use of boundary control with second-order switching surface to reduce the system order for deadbeat controller in grid-connected inverter," *IEEE Trans. Power Electron.*, vol. 31, no. 3, pp. 2638-2653, Mar. 2016.
- [10] Z. Liu, B. Zhang and K. Zhou, "Universal fraction-order design of linear phase lead compensation multirate repetitive control for PWM inverters," *IEEE Trans. Ind. Electron.*, vol. 64, no. 9, pp. 7132-7140, Sept. 2017.
- [11] N. M. and D. Prasad, "A modified feedback scheme suitable for repetitive control of inverter with non-linear load," *IEEE Trans. Power Electron.*, DOI 10.1109/TPEL.2017.2690361.
- [12] Y. Wang, A. Darwish, D. Holliday, and B. W. Williams, "Plug-in repetitive control strategy for high-order wide-output range impedance-source converters," *IEEE Trans. Power Electron.*, vol. 32, no. 8, pp. 6510-6522, Aug. 2017.
- [13] Y. Song and H. Nian, "Enhanced Grid-Connected Operation of DFIG Using Improved Repetitive Control Under Generalized Harmonic Power Grid," *IEEE Trans. Energy Convers.*, vol. 30, no. 3, pp. 1019-1029, Sept. 2015.
- [14] S. Madichetty, A. Dasgupta, S. Mishra, C. K. Panigrahi, and G. Basha, "Application of an advanced repetitive controller to mitigate harmonics in MMC with APOD scheme," *IEEE Trans. Power Electron.*, vol. 31, no. 9, pp. 6112-6121, Sep. 2016.
- [15] S. Yang, P. Wang, Y. Tang, and L. Zhang, "Explicit phase lead filter design in repetitive control for voltage harmonic mitigation of VSI-based islanded microgrids," *IEEE Trans. Ind. Electron.*, vol. 64, no. 1, pp. 817-826, Jan. 2017.
- [16] T. Q. Liu, D. W. Wang, and K. L. Zhou, "High-performance grid simulator using parallel structure fractional repetitive control," *IEEE Trans. Power Electron.*, vol. 31, no. 3, pp. 2669-2679, Mar. 2016.
- [17] H. Ma, J. Wu, and Z. Xiong, "A novel exponential reaching law of discrete-time sliding-mode control," *IEEE Trans. Ind. Electron.*, vol. 64, no. 5, pp. 3840-3850, May. 2017.
- [18] A. Marcos-Pastor, E. Vidal-Idiarte, A. C. Pastor, and L. M. Salamero, "Interleaved digital power factor correction based on the sliding-mode approach," *IEEE Trans. Power Electron.*, vol. 31, no. 6, pp. 4641-4653, Jun. 2016.
- [19] V. Repecho, D. Biel, J. M. Olm, and E. Fossas, "Switching frequency regulation in sliding mode control by a hysteresis band controller," *IEEE Trans. Power Electron.*, vol. 32, no. 2, pp. 1557-1569, Feb. 2017.
- [20] N. M. Dehkordi, N. Sadati, and M. Hamzeh, "A robust backstepping high-order sliding mode control strategy for grid-connected DG units with harmonic/interharmonic current compensation capability," *IEEE Trans. Sustain. Energy*, vol. 8, no. 2, pp. 561-572, Apr. 2017.
- [21] H. Ma, J. Wu, and Z. Xiong, "Discrete-time sliding-mode control with improved quasi-sliding-mode domain," *IEEE Trans. Ind. Electron.*, vol. 63, no. 10, pp. 6292-6304, Oct 2016.
- [22] R. Fantino, C. Busada, and J. Solsona, "Optimum PR control applied to LCL filters with low resonance frequency," *IEEE Trans. Power Electron.*, DOI: 10.1109/TPEL.2017.2667409.
- [23] Y. Zhang, J. Li, X. Li, Y. Cao, M. Sumner, and C. Xia, "A method for the suppression of fluctuations in the neutral-point potential of a three-level NPC inverter with a capacitor-voltage loop," *IEEE Trans. Power Electron.*, vol. 32, no. 1, pp. 825-836, Jan. 2017.
- [24] C. Citro, P. Siano, and C. Cecati, "Designing inverters' current controllers with resonance frequencies cancellation," *IEEE Trans. Ind. Electron.*, vol. 63, no. 5, pp. 3072-3080, May 2016.
- [25] H. Komurcugil, N. Altin, S. Ozdemir, and L. Sefa, "Lyapunov-function and proportional-resonant-based control strategy for single-phase grid-connected VSI with LCL filter," *IEEE Trans. Ind. Electron.*, vol. 63, no. 5, pp. 2838-2849, May 2016.
- [26] X. A. Fu, and S. H. Li, "Control of single-phase grid-connected converters with LCL filters using recurrent neural network and conventional control methods," *IEEE Trans. Power Electron.*, vol. 31, no. 7, pp. 5354-5364, Jul. 2016.
- [27] A. Kuperman, "Proportional-resonant current controllers design based on desired transient performance," *IEEE Trans. Power Electron.*, vol. 30, no. 10, pp. 5341-5345, Oct. 2015.
- [28] M. J. Ryan and R. D. Lorenz, "A synchronous-frame controller for a single-phase sine wave inverter," in Proc. IEEE APEC, Feb. 1997, pp. 813-819.
- [29] A. Roshan, R. Burgos, A. C. Baisden, F. Wang, and D. Boroyevich, "A D-Q frame controller for a full-bridge single phase inverter used in small distributed power generation systems," in Proc. IEEE APEC, Feb. 2007, pp. 641-647.
- [30] B. Bahrani, A. Rufer, S. Kenzelmann, and L. Lopes, "Vector control of single-phase voltage source converters based on fictive axis emulation," *IEEE Trans. Ind. Appl.*, vol. 47, no. 2, pp. 831-840, Mar./Apr. 2011.
- [31] J. Chen, W. Zhang, B. Chen, and Y. Ma, "Improved vector control of brushless doubly fed induction generator under unbalanced grid

conditions for offshore wind power generation," *IEEE Trans. Energy Convers.*, vol. 31, no. 1, pp. 293–302, Mar. 2016.

- [32] A. Vidal, F. D. Freijedo, A. G. Yepes, J. Malvar, O. Lopez, and J. Doval-Gandoy, "Transient response evaluation of stationary-frame resonant current controllers for grid-connected applications," *IET Power Electron.*, 2014, vol. 7, no. 7, pp. 1714–1724.
- [33] S. G. Xu, J. P. Wang, and J. P. Xu, "A current decoupling parallel control strategy of single-phase inverter with voltage and current dual closed-loop feedback," *IEEE Trans. Ind. Electron.*, vol. 60, no. 4, pp. 1306–1313, Apr. 2013.
- [34] M. Monfared, S. Golestan, and J. M. Guerrero, "Analysis, design, and experimental verification of a synchronous reference frame voltage control for single-phase inverters," *IEEE Trans. Ind. Electron.*, vol. 61, no. 1, pp. 258–269, Jan. 2014.
- [35] Y. Han, Z. Li, P. Yang, C. Wang, L. Xu and J. Guerrero, "Analysis and design of improved weighted average current control strategy for LCL-type grid-connected inverters," *IEEE Trans. Energy Convers.*, vol. 32, no. 3, pp. 941–952, Feb. 2017.
- [36] Zhang X, Spencer J W, Guerrero J M, "Small-signal modeling of digitally controlled grid-connected inverters with LCL filters," *IEEE Trans. Ind. Electron.*, vol. 60, pp.3752–3765, September 2013.
- [37] D. H. Pan, X. B. Ruan, X. H. Wang, H. Yu, and Z. W. Xing, "Analysis and design of current control schemes for LCL-Type grid-connected inverter based on a general mathematical model," *IEEE Trans. Power Electron.*, vol. 32, no. 6, pp. 4395–4410, Jun. 2017.
- [38] F. Bosio, L. A. S. Ribeiro, F. D. Freijedo, M. Pastorelli, and J. M. Guerrero, "Effect of state feedback coupling and system delays on the transient performance of stand-alone VSI with LC output filter," *IEEE Trans. Ind. Electron.*, vol. 63, no. 8, pp. 4909–4918, Aug. 2016.
- [39] S. Somkun, and V. Chankag, "Unified unbalanced synchronous reference frame current control for single-phase grid-connected voltage-source converters," *IEEE Trans. Ind. Electron.*, vol. 63, no. 9, pp. 5425–5436, Sept. 2016.
- [40] S. Kim, J. Im, E. Song, and R. Kim, "A new rotor position estimation method of IPMSM using all-pass filter on high-frequency rotating voltage signal injection," *IEEE Trans. Ind. Electron.*, vol. 63, no. 10, pp. 6499–6509, Oct. 2016.
- [41] B. Wang, Y. Xu, Z. Shen, J. Zou, C. Li, and H. Liu, "Current control of grid-connected inverter with LCL filter based on extended-state observer estimations using single sensor and achieving improved robust observation dynamics," *IEEE Trans. Ind. Electron.*, vol. 64, no. 7, pp. 5428–5439, Jul. 2017.
- [42] C. L. Bao, X. B. Ruan, X. H. Wang, W. W. Li, D. H. Pan, and K. L. Weng, "Step-by-step controller design for LCL-type grid-connected inverter with capacitor-current-feedback active-damping," *IEEE Trans. Power Electron.*, vol. 29, no. 3, pp. 1239–1253, Mar 2014.



**Yang Han** (S'08-M'10-SM'17) received the Ph.D. in Electrical Engineering from Shanghai Jiaotong University (SJTU), Shanghai, China, in 2010. He joined the Department of Power Electronics, School of Mechatronics Engineering, University of Electronic Science and Technology of China (UESTC) in 2010, and has been an Associate Professor since 2013. From March 2014 to March 2015, he was a visiting scholar (guest postdoc) in the area of renewable energy and microgrids at the Department

of Energy Technology, Aalborg University, Aalborg, Denmark. His research interests include AC/DC microgrids, grid-connected converters for renewable energy systems and DGs, phase-locked loop (PLL), power quality, active power filters and static synchronous compensators (STATCOMs).

He has authored more than 20 ISI-indexed international journal papers and one book chapter in the area of power electronics, power quality conditioners, and smart grid. He has served as the Session Chair in "Microgrid Optimization and Scheduling" Session in the 2nd International Conference on Power and Renewable Energy (ICPRE) in Chengdu in 2017, and in "Power Quality Mitigation and Application" Session in the 5th National Conference on Power Quality in Xi'an in 2017, and in "AC/DC, DC/AC Power Converter" Session in the 2016 IPEMC ECCE-Asia in Hefei, China. He was awarded "Baekhyun Award" by the Korean Institute of Power Electronics (KIPE) in 2016. He received the Best Paper Awards from the 6th Asia International Symposium on Mechatronics in 2017, the 5th National Conference on Power Quality in 2017, the Annual Conference of HVDC and Power Electronics Committee of Chinese Society of Electrical Engineers (CSEE) in 2013, and the 4th International Conference on Power Quality in 2008. He has eighteen issued and ten pending

patents. He is an active reviewer for IEEE Transactions on Power Electronics, IEEE Transactions on Industrial Electronics, IEEE Transactions on Smart Grid, IEEE Transactions on Energy Conversion, and IEEE Industrial Electronics Magazine.



**Aiting Jiang** received the B.S. degree in Electrical Engineering and Automation from University of Electronic Science and Technology of China (UESTC), Chengdu, China, in 2016. She is currently working towards the M.S. degree in Power Electronics and Electric Drives at UESTC, Chengdu, China. Her current research interests include the optimization of stand-alone PWM converters, phase-locked loop (PLL) and power quality,



His research interests are Power-factor Correction, PV and Fuel Cell Systems, Microgrid Modelling and Digital Control by microcontrollers and DSP's.

**Ernane Antônio Alves Coelho** received the B.S. degree in electrical engineering from the Federal University of Minas Gerais, Belo Horizonte, Brazil, the M.S. degree from the Federal University of Santa Catarina, Florianopolis, Brazil, and the Ph.D. degree from the Federal University of Minas Gerais in 1987, 1989, and 2000, respectively. In 1989, he joined the Electrical Engineering Faculty at Federal University of Uberlandia, where he is currently a Full Professor. His research interests are Power-factor Correction, PV and Fuel Cell Systems, Microgrid Modelling and Digital Control by microcontrollers and DSP's.



2012 he is a guest Professor at the Chinese Academy of Science and the Nanjing University of Aeronautics and Astronautics; from 2014 he is chair Professor in Shandong University; from 2015 he is a distinguished guest Professor in Hunan University; and from 2016 he is a visiting professor fellow at Aston University, UK.

His research interests are oriented to different microgrid aspects, including power electronics, distributed energy-storage systems, hierarchical and cooperative control, energy management systems, smart metering and the internet of things for AC/DC microgrid clusters and islanded minigrids; recently specially focused on maritime microgrids for electrical ships, vessels, ferries and seaports. Prof. Guerrero is an Associate Editor for the IEEE TRANSACTIONS ON POWER ELECTRONICS, the IEEE TRANSACTIONS ON INDUSTRIAL ELECTRONICS, and the IEEE Industrial Electronics Magazine, and an Editor for the IEEE TRANSACTIONS ON SMART GRID and IEEE TRANSACTIONS ON ENERGY CONVERSION. He has been Guest Editor of the IEEE TRANSACTIONS ON POWER ELECTRONICS Special Issues: Power Electronics for Wind Energy Conversion and Power Electronics for Microgrids; the IEEE TRANSACTIONS ON INDUSTRIAL ELECTRONICS Special Sections: Uninterruptible Power Supplies systems, Renewable Energy Systems, Distributed Generation and Microgrids, and Industrial Applications and Implementation Issues of the Kalman Filter; the IEEE TRANSACTIONS ON SMART GRID Special Issues: Smart DC Distribution Systems and Power Quality in Smart Grids; the IEEE TRANSACTIONS ON ENERGY CONVERSION Special Issue on Energy Conversion in Next-generation Electric Ships. He was the chair of the Renewable Energy Systems Technical Committee of the IEEE Industrial Electronics Society. He received the best paper award of the IEEE Transactions on Energy Conversion for the period 2014–2015. In 2014 and 2015 he was awarded by Thomson Reuters as Highly Cited Researcher, and in 2015 he was elevated as IEEE Fellow for his contributions on "distributed power systems and microgrids."